LIDAR CALIBRATION OF SATELLITE SENSED CDOM IN THE SOUTHERN OCEAN

Luca Fiorani[1], Roberta Fantoni[1], Luigi Lazzara[2], Ilaria Nardello[2], Igor Okladnikov[3] and Antonio Palucci[1]

1. ENEA, Via Fermi 45, 00044 Frascati, Italy; fiorani(at)frascati.enea.it
2. University of Florence, 50125 Florence, Italy
3. SCERT, Akademicheskii Avenue 10/3, 634055 Tomsk, Russia

ABSTRACT

Chromophoric dissolved organic matter (*CDOM*) is a key parameter in the biogeochemical cycles affecting the oceans' contribution to the carbon budget of the Earth system. Despite its importance, important ocean colour satellite radiometers do not provide *CDOM* as a standard product.

Within this framework, we are presenting a lidar-calibrated *CDOM* algorithm for satellite imagery. It is based on the data collected by the ENEA Lidar Fluorosensor onboard the research vessel *Italica* during the 18th Italian Antarctic Oceanographic Campaign carried out from 5 January to 5 March 2003 in the Ross Sea.

Although the results are preliminary, they provide valuable information on distribution and dynamics of *CDOM* in the Southern Ocean, one of the less studied but more interesting zones of our planet from a biological point of view because of a series of circumpolar fronts that result in the definition of different oceanographic provinces, where the development of endemic phytoplankton is favoured.

Keywords: Lidar fluorosensor, satellite radiometer, CDOM, chromophoric dissolved organic matter, Southern Ocean.

INTRODUCTION

Organic carbon in the world oceans is present mainly as dissolved organic matter (*DOM*) and a large part of it is chromophoric *DOM* (*CDOM*) (1): Therefore, investigating the distribution and dynamics of *CDOM* will help us understand the global carbon cycle.

In addition, *CDOM* is directly linked to phytoplankton at least in two ways. On the one hand, *CDOM* limits light penetration into seawater and, as a consequence, regulates algal growth (2). On the other hand, phytoplankton exudation and degradation in algal blooms can increase CDOM concentration (1).

A third reason to study *CDOM* is that it is correlated with dymethyl sulphide (3), a climate-driving factor, through a feedback process controlled by phytoplankton (4), which cannot be directly measured by present ocean colour satellite radiometers. *CDOM* is not among the data products provided by important satellite radiometers, either; e.g., a standard *CDOM* algorithm is not available for the Sea-viewing Wide Field-of-view Sensor (SeaWiFS) (5), although the SeaWiFS Project Office recognized its usefulness (6). Nevertheless, some algorithms have been suggested for calculating the *CDOM* absorption coefficient from ocean colour data products (7,8,9,10,11).

To sum it up it can be said that *CDOM* is a key oceanic variable and the debate on its satellite retrieval is still open: This explains our research effort in calibrating a *CDOM* algorithm for the water-leaving radiance data collected by space-borne radiometers. Such an algorithm has been developed based on the measurements carried out by the ENEA Lidar Fluorosensor (12) onboard the research vessel *Italica* during the 18th Italian Antarctic Oceanographic Campaign performed from 5 January to 5 March 2003 in the Ross Sea, with particular emphasis on coastal zones and polynya areas. The ENEA Lidar Fluorosensor is based on laser-induced fluorescence and continuously

provides concentrations of *CDOM* and phytoplankton pigments all along the ship track. The approach of this study is similar to that followed for a lidar-calibrated chlorophyll *a* (*Chl-a*) algorithm (13), but requires the *CDOM* absorption coefficient to be retrieved from fluorescence measurements (14). Although the present results are preliminary, they provide valuable information on the distribution and dynamics of *CDOM* in the Southern Ocean.

METHODS

Details and references on SeaWiFS, ENEA Lidar Fluorosensor and Chl-a algorithms can be found in previous publications (5,12,13). Here, we are reviewing the main characteristics of the ENEA Lidar Fluorosensor in Table 1 and we are focusing on the lidar calibration of the *CDOM* algorithm.

Table 1. Specifications of the ENEA Lidar Fluorosensor.

Transmitter	Wavelength	355 nm
	Pulse energy	3 mJ
	Pulse duration	10 ns
	Pulse repetition rate	10 Hz
Receiver	Clear aperture	0.4 m
	Focal length	1.65 m
	Centre wavelengths	404, 450, 585, 680 nm
	Bandwidths	5 nm FWHM
Electronics	Detectors	Photomultipliers
	Gate width	100 ns
	Dynamic range	15 bit
	Central processing unit	VME embedded 486

The lidar optical channels at 404 and 450 nm correspond to Raman scattering of water and fluorescence of *CDOM*, respectively, and the *CDOM* fluorescence signal (f_{CDOM}) is released in normalised units (*NU*), i.e., it is normalised to the water Raman scatter peak (12). Afterwards, it is converted into *CDOM* absorption (a_{CDOM}) by calibration with measurements carried out with the absorption and attenuation meter WET Labs AC-9[1]. The ENEA Lidar Fluorosensor and AC-9 operated simultaneously in some stations of the oceanographic campaign. AC-9 determined spectral attenuation and absorption on samples of filtered seawater over nine wavelengths: 412, 440, 488, 510, 555, 630, 650, 676 and 715 nm. At 412 and 440 nm, absorption of filtered seawater corresponds to a_{CDOM}, because other effects are negligible for wavelengths below 500 nm (7,15).

The best correlation between f_{CDOM} and a_{CDOM} has been found at 440 nm: This explains why a_{CDOM} at 440 nm is used to calibrate f_{CDOM} (emission at 440 nm). The final results of the lidar calibration are given in Figure 1 and Table 2. Statistical data processing can be found in (16).

Table 2. Results of the calibration of the ENEA Lidar Fluorosensor by AC-9 (a_1 is the slope, σ_1 is the slope error and R is the correlation coefficient).

# of points	a_1	σ_1	R
35	0.0517	0.0030	0.74

---

[1] Van Zee H & I Walsh, 2004. <u>AC-9 Specification Sheet</u> (Wet LABS, Philomath).
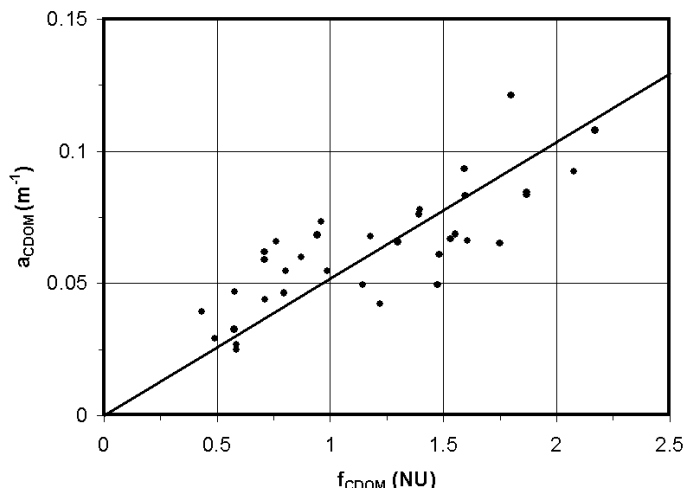
Figure 1: Calibration of the ENEA Lidar Fluorosensor by AC-9.

Lidar *CDOM* data, now expressed in m^{-1}, can be used for the lidar calibration of the SeaWiFS *CDOM* algorithm exactly in the same way lidar Chl-a data has been used for the lidar calibration of the SeaWiFS Chl-a algorithm, as already described in a previous publication (13). The only difference is that normalised water leaving radiance (*Lwn*) at 443 and 510 nm is employed instead of that at 490 and 555 nm. The rationale of choosing those wavelengths is that a_{CDOM} is strong at 443 nm and weak at wavelengths greater than 500 nm (15). The use of *Lwn*(412 nm) has been avoided because of problems with atmospheric correction at short wavelengths (17). The *Lwn*(510 nm) channel has been preferred to the *Lwn*(555 nm) channel, because it is less affected by suspended inorganic material (5). Also in this case, only the final results of the SeaWiFS calibration are given (Figure 2 and Table 3). Statistical data processing can be found in (16). Here we observe only that the lidar *CDOM* data are fitted on the SeaWiFS band ratios Lwn(443)/Lwn(510) in a log-log plot, thus providing an algorithm for the retrieval of *CDOM* from radiance as in common *Chl-a* bio-optical algorithms.

Table 3. Results of the calibration of SeaWiFS by the ENEA Lidar Fluorosensor; a_0 is the intercept, σ_0 is the intercept error, a_1 is the slope, σ_1 is the slope error and R is the correlation coefficient.

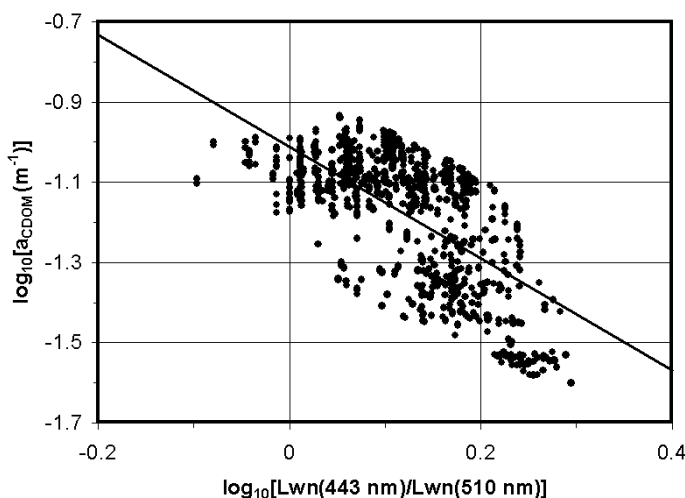| # of points	a_0	σ_0	a_1	σ_1	R
899	-1.0115	0.0074	-1.393	0.054	0.69

Figure 2: Calibration of SeaWiFS by the ENEA Lidar Fluorosensor.

In principle, it could have been possible to directly calibrate SeaWiFS by AC-9 but, in practice, the procedure followed here has two advantages:

- Lidar data are more suitable to that purpose than AC-9 samplings, because their geographic coverage and spatial resolution are closer to image extent and pixel size, respectively, of the SeaWiFS data products. In fact, a SeaWiFS pixel covers a large area (size ~10 km) and integrates information from 0 to ~10 m. While an AC-9 sampling is a point, after averaging the laser shots (repetition rate: 10 Hz, footprint: 0.1 m) in a SeaWiFS pixel, lidar data represent a track (length ~1 – 10 km, width ~0.1 m) of water column measurements (from 0 to ~10 m). On the contrary, in campaign stations where AC-9 samplings were performed, lidar and AC-9 measure nearly the same water because the ship stops.

- The number of lidar measurements is much larger than the number of AC-9 stations.

RESULTS

The lidar calibration of the SeaWiFS algorithm for CDOM and Chl-a has been carried out in the Ross Sea Region, i.e. the area delimited by the coast and a line (straight in the cylindrical equidistant projection) from a point near Cape Adare (72°S, 170°E) to a point near Cape Colbeck (76°S, 158°W). Although the Ross Sea Region does not coincide exactly with the Ross Sea, its simple definition was a necessary compromise: the calculation of the bio-optical properties in the Ross Sea Region rather than in the Ross Sea saves computing time because the satellite products are usually delivered in the cylindrical equidistant projection and it is easy to determine whether a pixel is above or below a straight line.

An example of the results obtained during the 18th Italian Antarctic Oceanographic Campaign (5 January – 5 March 2003) with level 3 8-day standard mapped image products is shown in Figure 3, where the continuous line represents the ship track. All the results obtained with 8-day products from 1 January to 5 March 2003 can be found in (16).
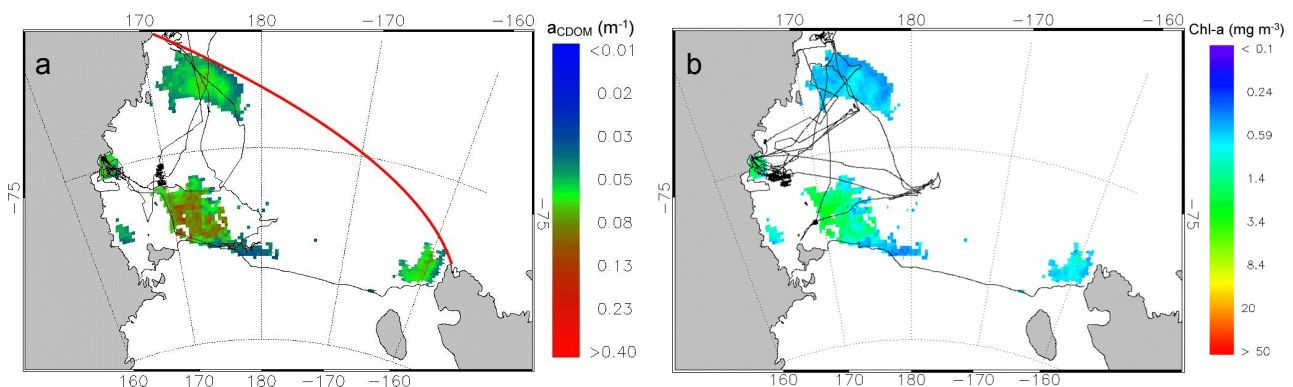

Figure 3: a_{CDOM} (a) and Chl-a (b) measured with the lidar-calibrated SeaWiFS algorithms in the Ross Sea Region during the period 01 – 08 January 2003. The Ross Sea Region is the area delimited by the coast and the continuous red line (indicated only on the left) from a point near Cape Adare (72°S, 170°E) to a point near Cape Colbeck (76°S, 158°W). That line is straight in cylindrical equidistant projection, used in SeaWiFS products, and curved in south polar stereographic projection, used in this figure. Missing pixels below the red line are due to sea ice or cloud cover. The continuous black line is the ship track: Concomitant lidar and SeaWiFS data are obtained where that line is superimposed to the satellite pixels.

In general, the values of a_{CDOM} found in this study compare quite well with data from the literature of the Ross Sea. In particular they are:

- Higher than the measurements taken in a former oceanographic campaign carried out in 1997 (18) and reported in Table 3.

- Similar to the values of a semi-analytical algorithm applied to SeaWiFS data in 1998 (about 0.1 m^{-1}) (10).

- Lower than the results of an empirical algorithm relative to SeaWiFS data in a 7-year period from 1997 to 2004 (around 0.2 m^{-1}) (19).

Table 3. a$_{CDOM}$ measured during the AESOPS (at 442 nm) and 18th Italian Antarctic (at 440 nm) oceanographic campaigns.

Oceanographic campaign	Mean / m^{-1}	Standard deviation / m^{-1}	Maximum / m^{-1}	Minimum / m^{-1}	# of stations	Period	Zone
AESOPS	0.027	0.021	0.140	0.001	40	09/11/97 14/03/98	53°S – 77°S 169°E – 166°W
18th Italian Antarctic	0.075	0.033	0.176	0.047	26	05/01/03 05/03/03	53°S – 78°S 164°E – 177°W

Because of the spatial and temporal evolutions of CDOM, it is difficult to understand how the comparison can be validated. The discrepancy between the AESOPS and 18th Italian Antarctic oceanographic campaigns can be explained by their temporal difference: The Italian survey took place in the more productive period of the Austral summer 2002-2003, while the American one encompasses almost all the Austral summer 1997-1998. This is confirmed by the larger variability of the AESOPS sample. For the last two points, it should be observed that the outcome of those algorithms is an average map of CDOM in the world oceans, hardly comparable with the few pixels involved in this study.

Missing satellite pixels are explained by sea ice or cloud cover on free waters. According to the observation in the visible band and in the microwave region by the National Oceanic and Atmospheric Administration (NOAA) satellites OLS[2] and SSM/I[3], respectively, the cloud cover is the main obstacle to SeaWiFS imaging of the open ocean, while sea ice dominates near the Antarctic coast. By the way, although it is not relevant in the lidar calibration of SeaWiFS, it can be pointed out that the ENEA Lidar Fluorosensor has two advantages with respect to SeaWiFS: Firstly, it is not sensitive to clouds, because it is installed on the ship and, secondly, it carries out measurements also in polynyas. Although the Austral summer 2002-2003 was characterised by exceptionally large ice coverage, phytoplankton blooms develop in ice-free regions (near Terra Nova Bay and Ross Island). The relationship between *CDOM* and *Chl-a* is clearly noticeable in Figure 3.

In order to give an estimate of temporal dynamics and spatial distribution of *CDOM* and *Chl-a* over a longer period and in a wider zone, the lidar-calibrated SeaWiFS algorithms for CDOM and Chl-a have been applied from the launch of SeaWiFS (1997) in the Ross Sea Sector, defined as the zone of the Southern Ocean from the coast north of 50°S latitude in the 160°E – 130°W interval.

---

[2] http://www.ngdc.noaa.gov/dmsp/sensors/ols.html

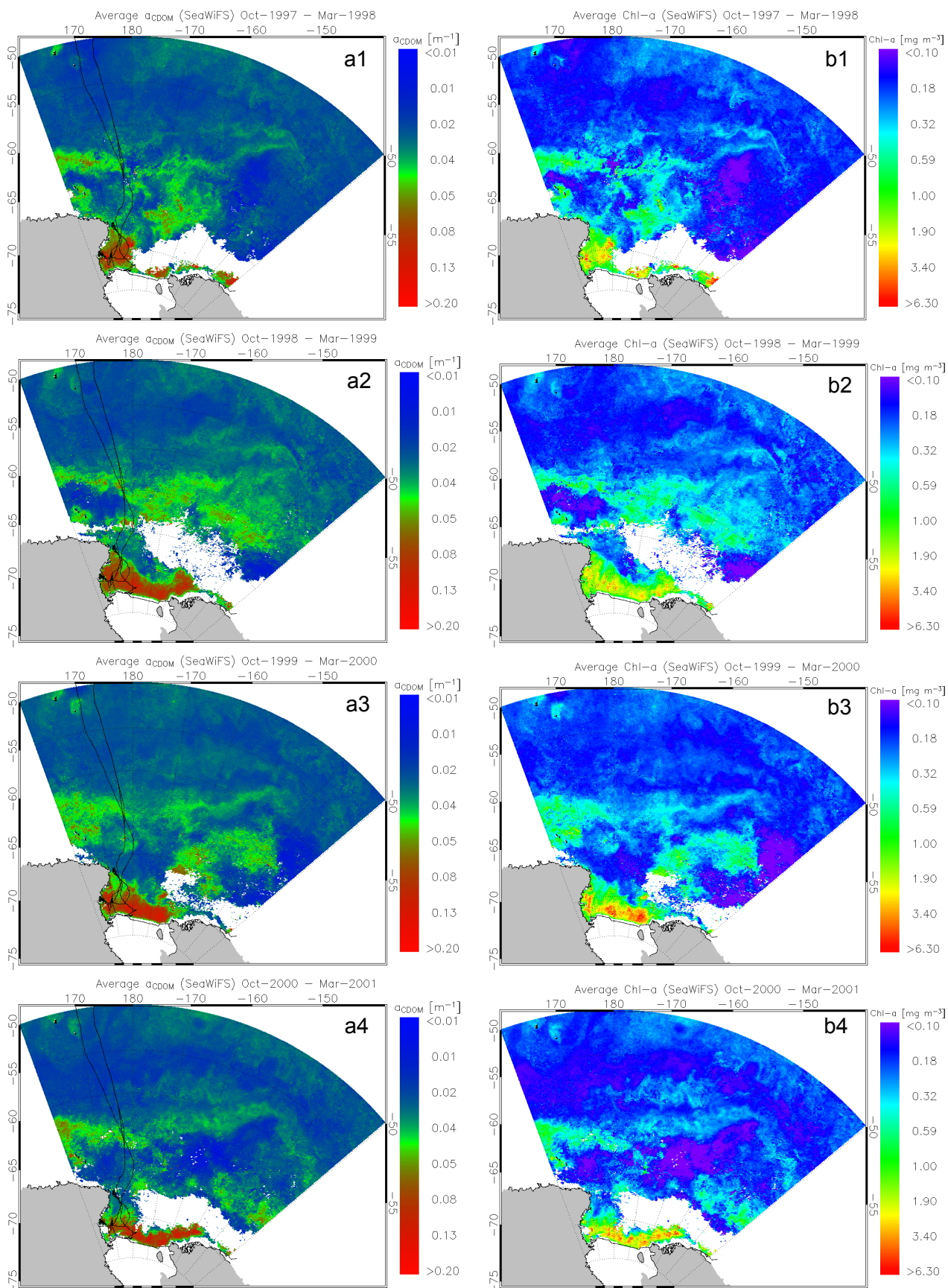[3] http://www.ngdc.noaa.gov/dmsp/sensors/ssmi.html

Figure 4: a_{CDOM} (a) and Chl-a (b) measured with the lidar-calibrated SeaWiFS algorithms in the Ross Sea Sector during the Austral summers from 1997-1998 (a1, b1), 1998-1999 (a2, b2), 1999-2000 (a3, b3), 2000-2001 (a4, b4), 2001-2002 (a5, b5), 2002-2003 (a6, b6) and 2003-2004 (a7, b7).
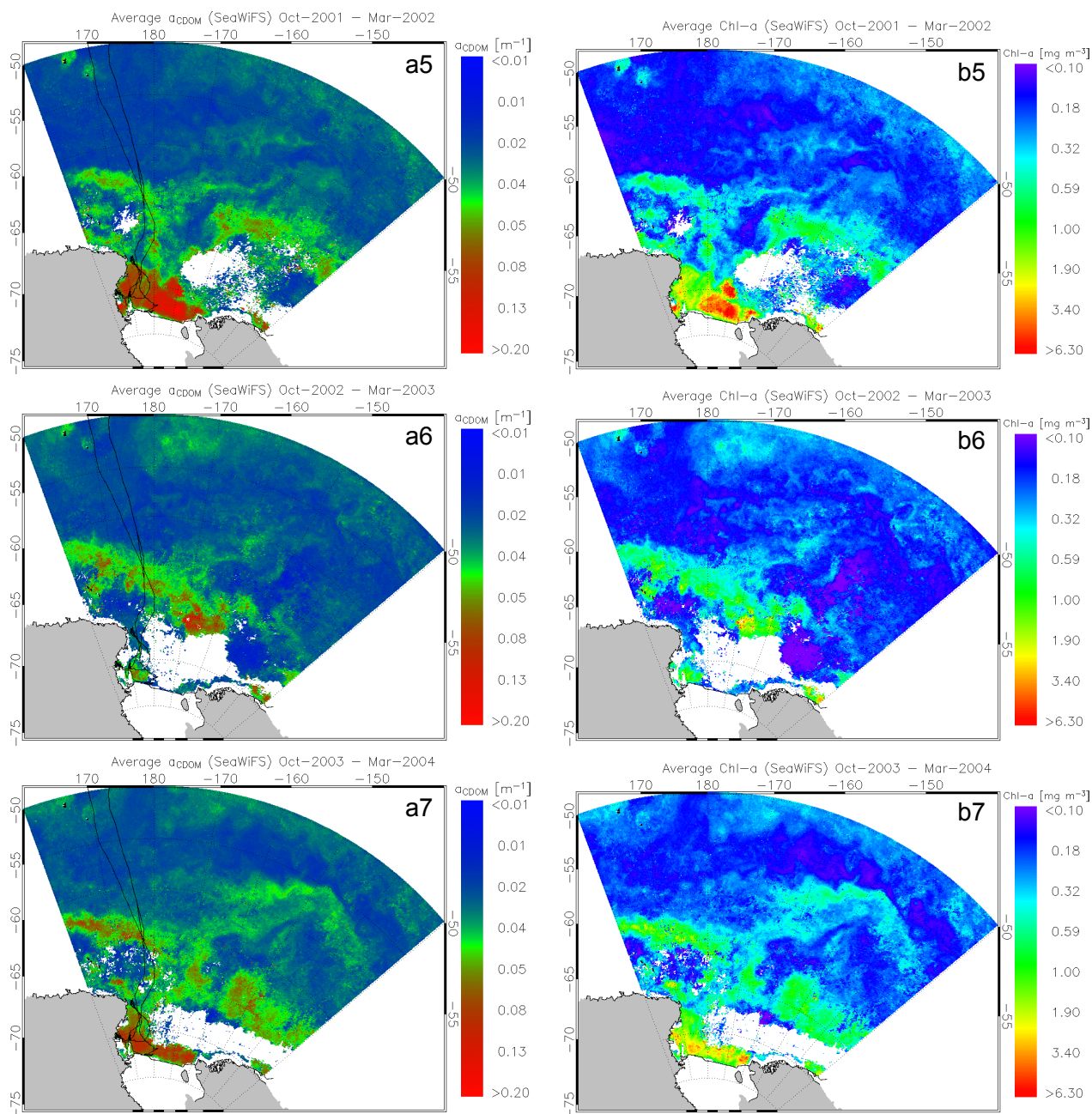
Figure 4 (continued).

The definition of the Ross Sea Sector has been chosen in order to compare our study with data from the literature (20). *CDOM* and *Chl-a* averaged during seven Austral summers (from 1997-1998 to 2003-2004) are shown in Figure 4. It is confirmed that Ross Sea is highly productive, especially near the Ross Ice Shelf. The larger *CDOM* and Chl-a in the open ocean are found in the Antarctic Divergence, an upwelling zone where nutrients are released. Ice coverage varies from year to year (e.g., it is low in 1999-2000 and high in 2002-2003), thus affecting the overall productivity. Nevertheless, it is confirmed that Ross Sea Region and Ross Sea Sector are quite productive in summer (1 – 2 mg m^{-3} in Ross Sea Region and 0.5 – 1 mg m^{-3} in Ross Sea Sector). Once more, the clear relationship between *CDOM* and *Chl-a* can be observed.

The behaviour of *CDOM* and *Chl-a* as well as their relationship can be studied in more detail when averaging *CDOM* and *Chl-a* in specific zones and observing their temporal dynamics. An example of such an investigation is given in Figure 5.
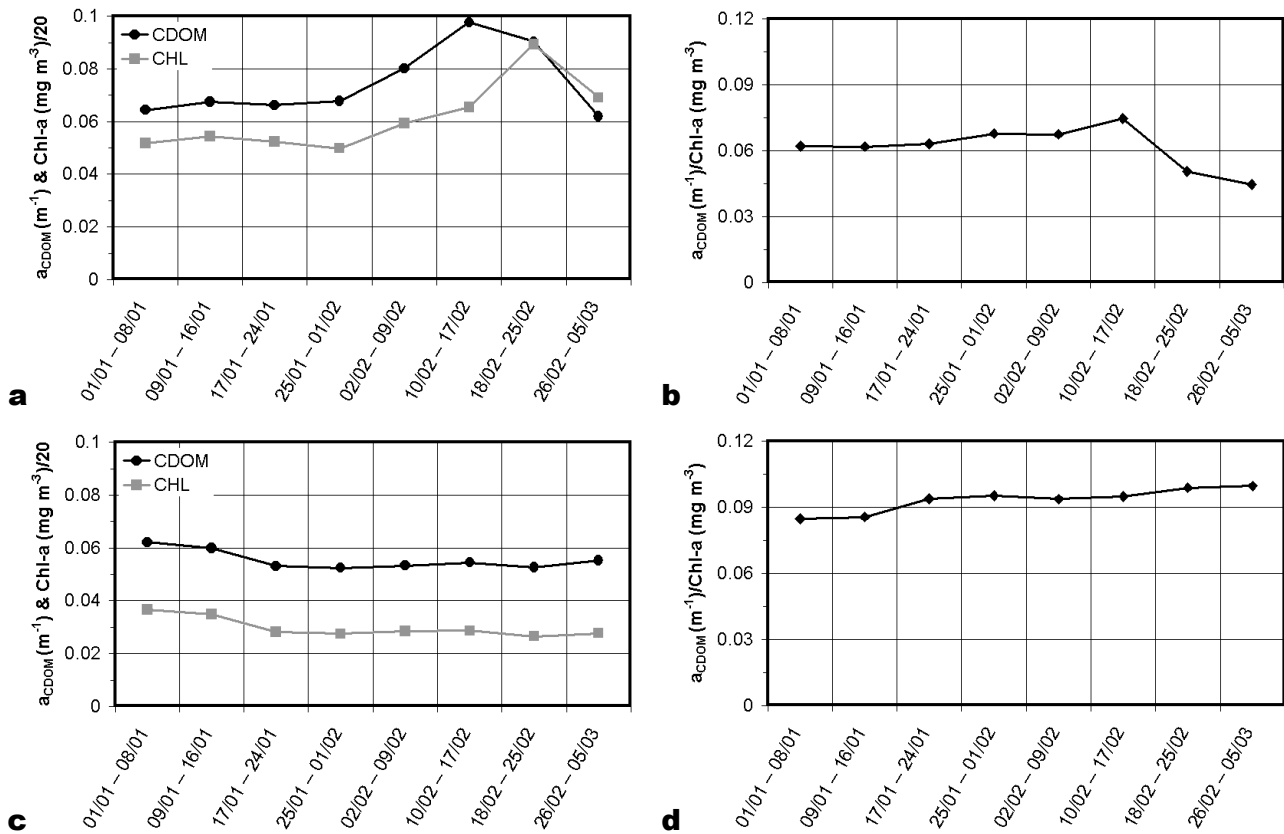
Figure 5: a_{CDOM} (black circles) and Chl-a (grey squares) averaged in Ross Sea Region (a) and their ratio (b) during the oceanographic campaign; a_{CDOM} (black circles) and Chl-a (grey squares) averaged in Ross Sea Sector (c) and their ratio (d) during the oceanographic campaign.

The correlation between *CDOM* and *Chl-a* is evident (*R* is 0.59 in Ross Sea Region and 0.97 in Ross Sea Sector). The average ratio between *CDOM* and *Chl-a* is different in Ross Sea Region (0.062 mg^{-1} m^2) and Ross Sea Sector (0.093 mg^{-1} m^2). This is probably due to the dissimilar taxonomic composition of Ross Sea Region and Ross Sea Sector. However, a common feature can be observed, in both Ross Sea Region and Ross Sea Sector: With some exceptions, the ratio is lower when *CDOM* and *Chl-a* are high. This behaviour could indicate two regimes: In the low ratio regime, *CDOM* could be dominated by the degradation product of phytoplankton metabolism, while in the high ratio regime, other sources could contribute to *CDOM* build-up (e.g. ice melting near the Ross Ice Shelf).

On the contrary, if a "bird flight view" of *CDOM* and *Chl-a* from 1997-1998 to 2003-2004 is required, contour plots of *CDOM* and *Chl-a* as a function of month of the year and Austral summer can be drawn, in both Ross Sea Region (Figure 6) and Ross Sea Sector (Figure 7).

In general, both *CDOM* and *Chl-a* are higher in the Ross Sea Region due to algal blooms in polynya regions. The maximum productivity was reached:

- in the Ross Sea Region in November 1998 (*Chl-a* ~ 7 mg m^{-3}),

- in the Ross Sea Sector in December 2001 (*Chl-a* ~ 1 mg m^{-3}).

It is confirmed that the exceptional ice coverage characterizing the Austral summer 2002-2003, severely limited algal development.

Although, once more, contour plots show a strong correlation between CDOM and *Chl-a*, it seems that the *CDOM* decay is generally slower than that of *Chl-a*: e.g. after the *Chl-a* peak in the Ross Sea Region in November 1998 (*Chl-a* ~ 7 mg m^{-3}), yet in December its value drops to ~ 2 mg m^{-3},

while a_{CDOM} is about constant in the same period. This could suggest that *CDOM* originates mainly from phytoplankton exudation and blooms degradation and is thus delayed in this case.
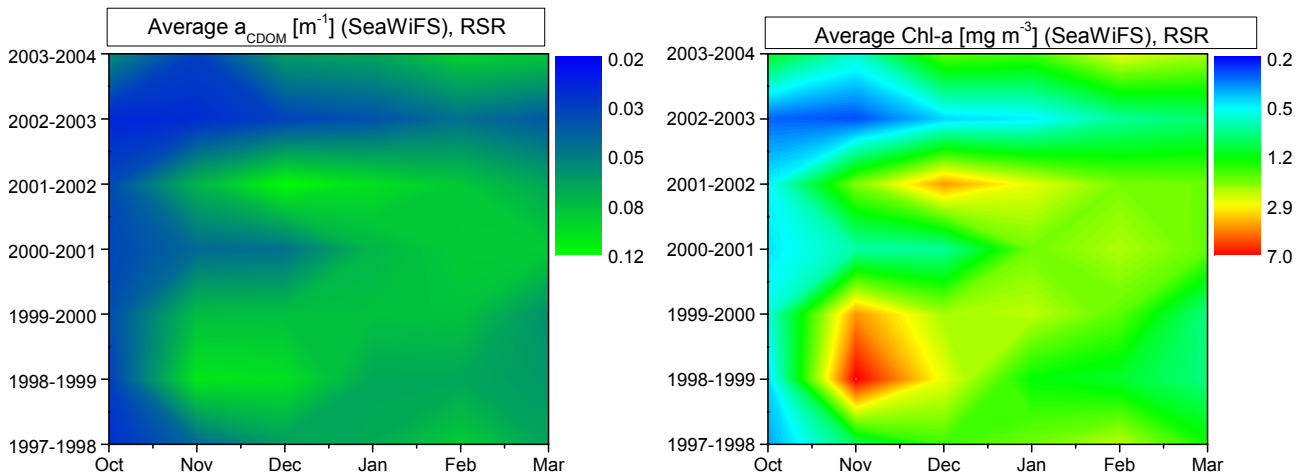

Figure 6: aCDOM *(left) and* Chl-a *(right) averaged in the Ross Sea Region as a function of month of the year and Austral summer.*
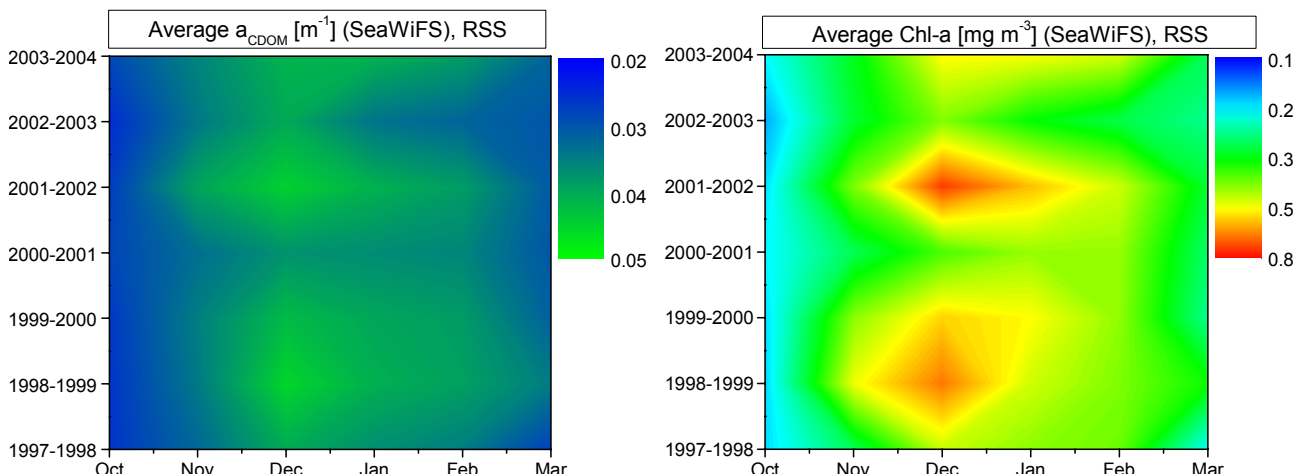

Figure 7: a_{CDOM} *(left) and* Chl-a *(right) averaged in the Ross Sea Sector as a function of month of the year and Austral summer.*

CONCLUSIONS

An original lidar-calibrated SeaWiFS algorithm for *CDOM* has been developed in the Ross Sea with the measurements of the 18th Italian Antarctic Oceanographic Campaign (Austral summer 2002-2003). The application of that algorithm to level 3 8-day standard mapped image SeaWiFS products in the Southern Ocean during the Austral summers from 1997-1998 to 2003-2004 provided a new series of estimates of a_{CDOM}(440 nm). The results of this study compare well with data from the literature, especially with recent values which are higher than those found in previous works. The interest of the approach followed in this study consists in the calibration of satellite data with in situ measurements. Moreover, using the ENEA lidar fluorosensor, this calibration was carried out all along the ship track and not only in the campaign stations.

Chl-a images have also been released owing to the application of a lidar-calibrated SeaWiFS algorithm for *Chl-a*. As a consequence, the evolution of *CDOM* and *Chl-a* were observed with various time resolutions (8-day, monthly, seasonal) in two different zones (Ross Sea and Ross Sea sector of the Southern Ocean), showing that the information on spatial distributions and temporal dynamics of both parameters improves our knowledge of the link between phytoplankton and *DOM*.

The data fusion between active and passive remote sensing, performed by ship-borne lidars and satellite-borne radiometers, respectively, allows a record of *CDOM* and *Chl-a* values to be gathered with an unprecedented spatial coverage and temporal extent. This approach helps us in understanding the contribution of the biogeochemical processes affecting the Southern Ocean to the global carbon cycle.

Future research will take advantage of the new ocean colour satellite radiometers Moderate Resolution Imaging Spectroradiometer (MODIS) (21) and Medium Resolution Imaging Spectrometer (MERIS) (22), in order to enlarge the lidar-calibrated SeaWiFS imagery of *CDOM* and *Chl-a*, and to build a long-term time series, which is necessary to assess the coupled ocean-atmosphere general circulation models that will help climate science to progress from description to prediction.

ACKNOWLEDGEMENTS

REFERENCES

1   Kirkpatrick G J, C Orrico, M A Moline, M Oliver & O M Schofield, 2003. Continuous hyperspectral absorption measurements of colored dissolved organic material in aquatic systems. Applied Optics, 42: 6564-6568

2   Olaizola M, R J Geider, W G Harrison, L M Graziano, G M Ferrari & P M Schlittenhardt, 1986. Synoptic study of variations in the fluorescence-based maximum efficiency of photosynthesis across the North Atlantic Ocean. Limnology and Oceanography, 41: 755-765

3   Toole D A, D A Siegel, D Slezak, R P Kiene, N B Nelson & J W Dacey, 2002. A light driven upper-ocean dimethylsulfide (DMS) biogeochemical cycling model for the Sargasso Sea. In: Proceedings of the AGU Fall Meeting, edited by R Wesson (AGU, San Francisco)

4   Toole D A & D A Siegel, 2004. Light-driven cycling of dimethylsulfide (DMS) in the Sargasso Sea: closing the loop. Geophysical Research Letters, 31: L09308

5   Hooker S B, W E Esaias, G C Feldman, W W Gregg & C R McClain, 1992. An overview of SeaWiFS and ocean color. In: SeaWiFS Technical Report Series, Volume 1, edited by S B Hooker & E R Firestone (NASA, Greenbelt) 25 pp.

6   McClain C R, G C Feldman & S B Hooker, 2004. An Overview of the SeaWiFS project and strategies for producing a climate research quality global ocean bio-optical time series. Deep-Sea Research II, 51: 5-42

7   Aiken J, G F Moore, C C Trees, S B Hooker & D K Clark, 1995. The SeaWiFS CZCS-type pigment algorithm. In: SeaWiFS Technical Report Series, Volume 29, edited by S B Hooker & E R Firestone (NASA, Greenbelt)

8   Hoge F E, C W Wright, P E Lyon, R N Swift & J K Yungel, 1999. Satellite retrieval of inherent optical properties by inversion of an oceanic radiance model: a preliminary algorithm. Applied Optics, 38: 495-504

9   Barbini R, F Colao, R Fantoni, L Fiorani & A Palucci, 2002. Lidar tuning of the SeaWiFS algorithms in the Antarctic Ross Sea: preliminary results. In: Proceedings of the 7th International

Conference on Remote Sensing for Marine and Coastal Environments, edited by B Petoskey (VERIDIAN, Miami)

10   Siegel D A, S Maritorena, N B Nelson, D A Hansell & M Lorenzi-Kayser, 2002. Global distribution and dynamics of colored dissolved and detrital organic materials. Journal of Geophysical Research, 107(C12): 3228

11   Johannessen S C, W L Miller & J J Cullen, 2003. Calculation of UV attenuation and colored dissolved organic matter absorption spectra from measurements of ocean color. Journal of Geophysical Research, 108(C9): 3301

12   Barbini R, F Colao, R Fantoni, A Palucci & S Ribezzo, 2001, Differential lidar fluorosensor system used for phytoplankton bloom and seawater quality monitoring in Antarctica. International Journal of Remote Sensing, 22: 369-384

13   Barbini R, F Colao, R Fantoni, L Fiorani & A Palucci, 2003. Lidar fluorosensor calibration of the SeaWiFS chlorophyll algorithm in the Ross Sea. International Journal of Remote Sensing, 24: 3205-3218

14   Hoge F E, A Vodacek, R N Swift, J K Yungel & N V Blough, 1995. Inherent optical properties of the ocean: retrieval of the absorption coefficient of chromophoric dissolved organic matter from airborne laser spectral fluorescence measurements. Applied Optics, 34: 7032-7038

15   Kahru M & B G Mitchell, 2001. Seasonal and nonseasonal variability of satellite-derived chlorophyll and colored dissolved organic matter concentration in the California Current. Journal of Geophysical Research, 106(C2): 2517-2529

16   Fantoni R, L Fiorani, A Palucci & I G Okladnikov, 2005. New algorithm for CDOM retrieval from satellite imagery. In: Technical Reports of the Italian Agency for New Technologies, Energy and the Environment, edited by A Renieri, Volume RT/2005/19/FIS (ENEA, Frascati) 20 pp.

17   Siegel D A, M Wang, S Maritorena & W Robinson, 2000, Atmospheric correction of satellite ocean color imagery: the black pixel assumption. Applied Optics, 39: 3582-3591

18   Mitchell G, 2003. AESOPS/NBP97-8. In: US JGOFS Process Study Data 1989-1998, Volume 1, edited by US JGOFS Data Management Office (Woods Hole Oceanographic Institution, U.S.A.)

19   Fichot C G & W L Miller, 2004. CDOM on the global scale: implementation of an improved algorithm (SeaUV) to 7 years of SeaWiFS data. In: Proceedings of Ocean Optics XVII, edited by S Ackleson (ONR, Fremantle, U.S.A.)

20   Arrigo K R, D Worthen, A Schnell & M P Lizotte, 1998. Primary production in Southern Ocean waters. Journal of Geophysical Research C, 103: 15587-15600

21   Esaias W E, M R Abbott, I Barton, O B Brown, J W Campbell, K L Carder, D K Clark, R H Evans, F E Hoge, H R Gordon, W M Balch, R Letelier & P J Minnett, 1998. An overview of MODIS capabilities for ocean science observations. IEEE Transactions on Geoscience and Remote Sensing, 36: 1250-1265

22   Huot J-P, H Tait, M Rast, S Delwart, J-L Bézy & G Levrini, 2002. The optical imaging instruments and their applications: AATSR and MERIS. ESA Bulletin, 106: 56-66